Pergamon

Acta metall. mater. Vol. 42, No. 3, pp. 893–911, 1994

0956-7151/94 $6.00 + 0.00

DUCTILE-REINFORCEMENT TOUGHENING IN γ-TiAl INTERMETALLIC–MATRIX COMPOSITES: EFFECTS ON FRACTURE TOUGHNESS AND FATIGUE-CRACK PROPAGATION RESISTANCE

K. T. VENKATESWARA RAO[1], G. R. ODETTE[2] and R. O. RITCHIE[1]

[1]Department of Materials Science and Mineral Engineering, University of California, Berkeley, CA 94720 and [2]Materials Department, College of Engineering, University of California, Santa Barbara, CA 93106, U.S.A.

(Received 30 June 1993)

Abstract—The influence of the type, volume fraction, thickness and orientation of ductile phase reinforcements on the room temperature fatigue and fracture resistance of γ-TiAl intermetallic alloys is investigated. Large improvements in toughness compared to monolithic γ-TiAl are observed in both the TiNb- and Nb-reinforced composites under monotonic loading. Toughness increases with increasing ductile phase content, reinforcement thickness and strength; orientation effects are minimal. Crack-growth behavior is characterized by steep resistance curves primarily due to crack trapping/renucleation and extensive crack bridging by the ductile-phase particles. In contrast, under cyclic loading the influence of ductile phases on fatigue resistance is strongly dependent upon reinforcement orientation. Compared to monolithic γ-TiAl, improvements in fatigue-crack growth resistance are observed in TiNb-reinforced composites only in the face (C–L) orientation; crack-growth rates for the edge (C–R) orientation are actually faster in the composite. In comparison, Nb-particle reinforcements offer less toughening under monotonic loading but enhance the fatigue properties compared to TiNb reinforcements under cyclic loading.

1. INTRODUCTION

Titanium aluminide alloys based on the ordered intermetallic compound γ-TiAl ($L1_0$ structure) are currently of considerable interest as advanced high-temperature structural materials, owing primarily to their higher specific modulus, greater elevated-temperature strength and better oxidation resistance compared to conventional titanium alloys, superalloys and α_2-Ti_3Al based intermetallic alloys [1–7]. The alloys are currently being developed as potential materials for use in the cooler compressor sections of high-performance turbine engines and for skin structures of hypersonic and high-speed civil transport vehicles. However, the application of monolithic γ-TiAl is severely limited by its relatively low tensile ductility (<2%) and fracture toughness (~ 8 MPa$\sqrt{m}$) at ambient temperatures. Accordingly, much work in recent years has focused on obtaining an understanding of the structure–property relationships in these alloys and in improving their ductility and fracture resistance.

Both alloy modification (intrinsic) and compositing (extrinsic) approaches to toughening γ-TiAl have been explored [3–11]. Microalloying with elements such as V, Cr, Mn, Mo and Nb and optimized thermomechanical processing treatments have led to toughened dual-phase microstructures composed of alternating microlaminae of γ (TiAl) and α_2 (Ti_3Al). In this case, toughening contributions arise from an intrinsic change in the deformation mechanism, i.e. mechanical twinning of the γ-phase [7], as well as crack deflection and blunting at γ/α_2 or γ/γ interfaces, and shear-ligament bridging by the more ductile α_2 phase [4–7].

Composite approaches to toughening have centered around reinforcing TiAl with small volume fractions of ductile Nb, TiNb or Ti–6Al–4V particles [8–11]. The primary objective is to enhance toughness by crack-tip shielding arising from tractions provided by unbroken ductile ligaments bridging the crack wake, akin to approaches first proposed for brittle ceramics [12–14]. When the length of the bridging zone is *very* small compared to the specimen and crack length dimensions, the toughness increases with crack extension up to a maximum steady-state level, K_{SSB}, associated with the development of a steady-state bridging zone length, L_{SSB}. At this small-scale bridging limit, K_{SSB}, is given as [11]

$$K_{SSB} = \sqrt{K_t^2 + E' f t \sigma_0 \chi} \qquad (1)$$

where K_t is the critical crack-tip stress intensity factor required for crack initiation, E' is the plane-strain elastic modulus of the composite [$= E/(1-\nu^2)$, ν being the Poisson's ratio], σ_0, f, and t refer to the yield strength, volume fraction and characteristic dimension of the reinforcement, respectively. The non-dimensional work of rupture, χ, is the area under the

normalized-reinforcement stress $[\sigma(u)]$-displacement (u) function, defined as [13]

$$\chi = \int_0^{u^*/t} \left[\frac{\sigma(u)}{\sigma_0}\right] \mathrm{d}\left(\frac{u}{t}\right) \qquad (2)$$

where u^* is the critical crack-opening displacement at the point of reinforcement rupture. The characteristic dimension, t, is appropriately defined based on the reinforcement geometry, i.e. the diameter of a fiber, the average diameter of circle inscribing a sphere, and the thickness of a foil (lamina) or a pan-cake shaped reinforcement. Typical values of χ for γ-TiAl reinforced with Nb or Nb-alloys range between 0.9 to 1.5. Much larger values of χ, up to 4 or more, can be obtained using strain-hardening reinforcements that undergo extensive debonding from the matrix [9]. For nominal values of $\chi = 1.2$, $\sigma_0 = 400$ MPa and $t = 100\ \mu$m, the addition of a mere 20 vol.% of ductile particles ($f = 0.2$) yields K_{SSB} values of about 44 MPa$\sqrt{\text{m}}$, over five times the nominal TiAl toughness of 8 MPa$\sqrt{\text{m}}$. Additional toughening mechanisms include crack trapping, crack renucleation, crack deflection and branching, and process-zone phenomena such as microcracking and twinning. Many of these latter contributions are incorporated into K_t, which is larger than the intrinsic K_{ic} toughness of the brittle γ-TiAl matrix.

Despite the success in toughening γ-TiAl with ductile-phase reinforcements, the composites may have lower crack-growth resistance under cyclic fatigue conditions [15, 16] than monolithic γ-TiAl, as illustrated in Fig. 1. Under monotonic loads, the γ-TiAl + 10 vol.% TiNb composite exhibits an initiation toughness of about 16 MPa$\sqrt{\text{m}}$, nearly twice that of pure γ-TiAl [Fig. 1(a)]; the fracture resistance increases with further crack extension (referred to as resistance-curve or R-curve behavior) primarily due to bridging by unbroken TiNb ligaments in the crack wake [Fig. 1(b)]. In contrast, the diminished role of crack bridging under cyclic loads due to subcritical fatigue failure of the ductile TiNb phase [Fig. 1(d)], can lead to marginally faster crack velocities in

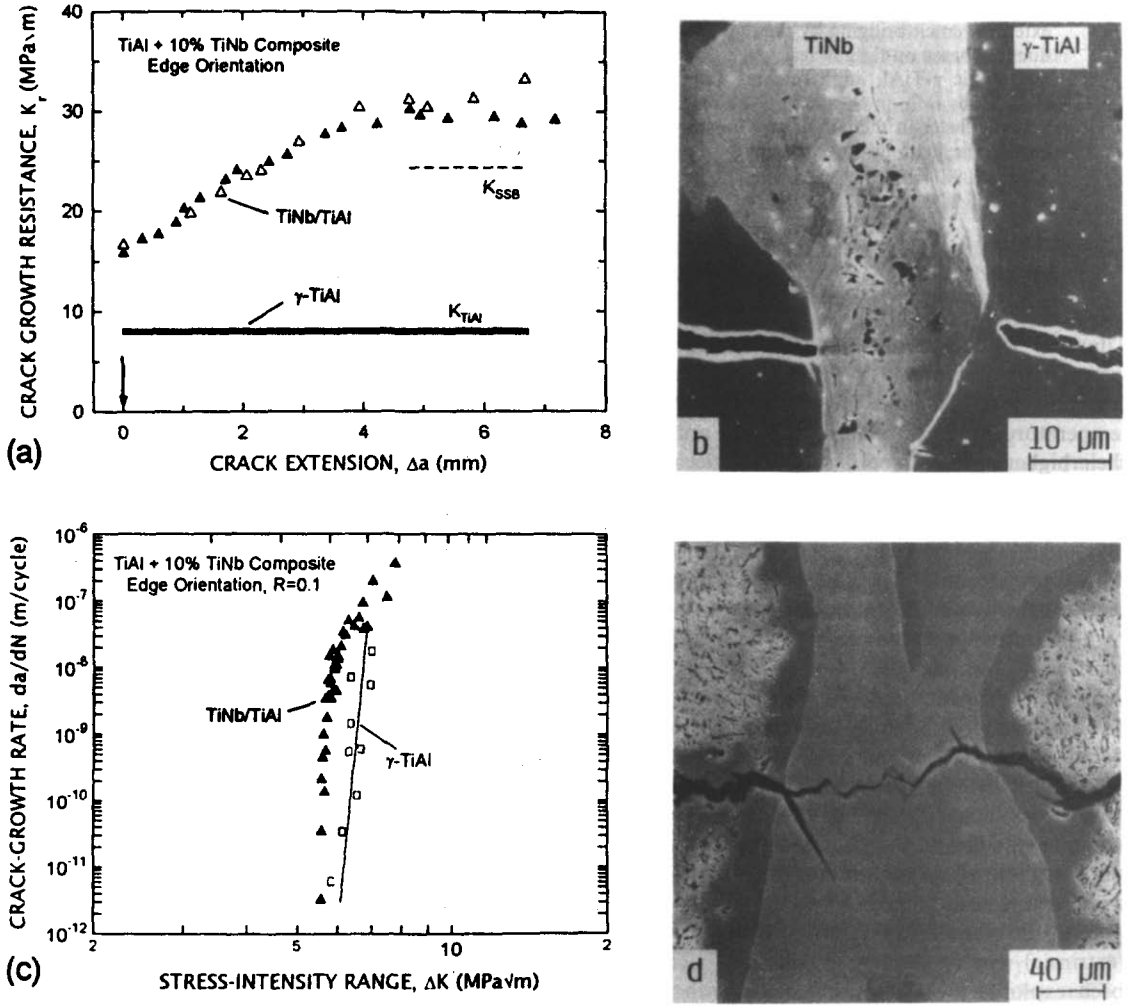

Fig. 1. Illustration of the contrasting role of ductile reinforcements on crack-growth behavior in a β-TiNb/γ-TiAl composite, showing (a) improved toughness compared to γ-TiAl under monotonic loading, due to (b) crack bridging by uncracked TiNb ligaments, and (c) faster growth rates in the composite under cyclic loading, (d) due to premature failure of the TiNb particles [after Ref. 15].

the composite compared to unreinforced TiAl [Fig. 1(c)].

Accordingly, it is the objective of the present paper to provide an extensive evaluation of ductile-phase toughening in γ-TiAl intermetallic-matrix composites by systematic measurements of the influence of volume fraction, thickness, orientation and type of reinforcement on their fatigue and fracture toughness properties. Specifically, a comparison of Nb and TiNb ductile phases provides the opportunity to evaluate the effects of widely different interface and reinforcement constitutive properties on the monotonic and cyclic crack-growth resistance of ductile-phase toughened composites.

2. MATERIALS AND EXPERIMENTAL PROCEDURES

2.1. Materials and fabrication

The ductile-phase toughened composites under study, listed in Table 1, were fabricated by phase blending -80 mesh γ-TiAl (Ti-55 at.% Al, with small additions of Nb, Ta, C and O) with various amounts of single-phase β-TiNb (Ti–33 at.% Nb) or pure Nb powders of $-35+50$ mesh (nominal size $\sim$300–500 μm) or $-50+140$ mesh (nominal size $\sim$100–300 μm). The blends were hot pressed and forged to upset ratios of 10:1 at 1025 ± 15°C, producing a pancake-shaped ductile particle morphology. Assuming a uniform thickness of $\sim$10% of the particle diameter, the nominal aspect ratio of the pancaked reinforcements is about 5:1 and the nominal particle thicknesses are $\sim$40 and $\sim$20 μm for $-35+50$ and $-50+140$ mesh powders, respectively.

The actual microstructures, however, were much more heterogeneous, as illustrated in Figs 2 and 3, and consisted of a distribution of irregularly shaped, lenticular-crenulated particles. Volume fractions and characteristic dimensions of the ductile particles varied, both between specimens and locally within a specimen. Measurements along the cracked edge and on the fracture surface of representative specimens (Fig. 3) showed a rather wide range of particle thicknesses (between 50 and 150% of nominal values) and aspect ratios in part due to the particle-size distribution and irregularities in particle shape. Furthermore, unusually thick reinforcements resulted when two particles were welded during processing, more frequently so at the higher volume fractions. Local fracture-surface area fractions of the ductile phase, taken along 500 μm slices, were found to vary by up to a factor of 2; however, specimen averages were generally within a few percent of the nominal values. Henceforth, the discussions will reference nominal reinforcement parameters, recognizing that these are surrogate measures for more complex distributions.

Table 1. Details of ductile-phase toughened γ-TiAl composites

Reinforcement	Mesh size	Nominal reinforcement volume fraction	Nominal reinforcement thickness (μm)
TiNb	$-35+50$	0.05	40
TiNb	$-35+50$	0.10	40
TiNb	$-35+50$	0.20	40
TiNb	$-50+140$	0.20	20
Nb	$-35+50$	0.20	40

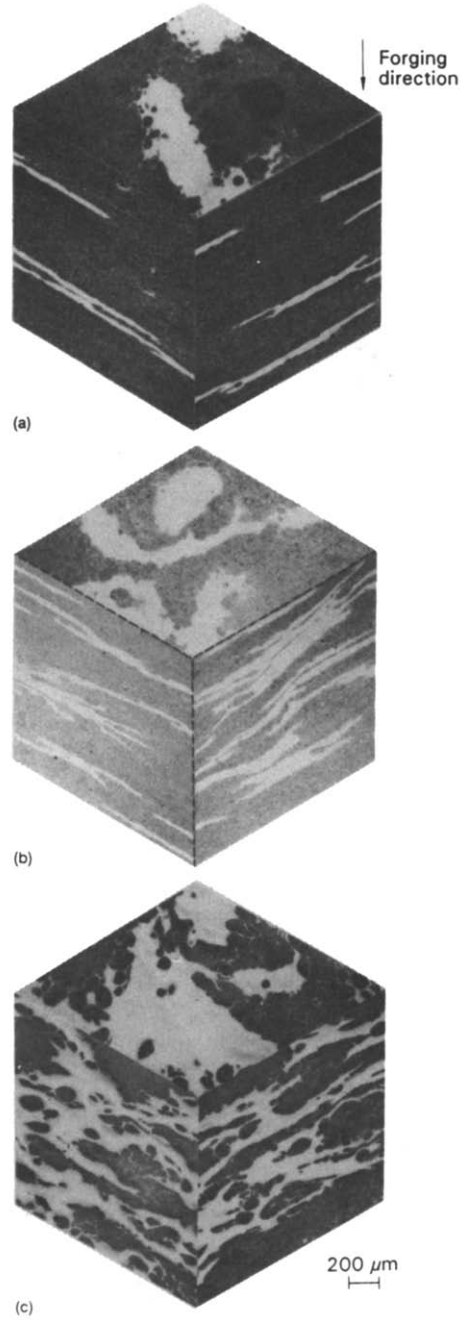

Fig. 2. Three-dimensional optical micrographs of typical γ-TiAl intermetallic–matrix composite microstructures reinforced with (a) 5 vol.%, (b) 10 vol.%, and (c) 15 vol.% of TiNb phase; the TiNb particle thickness is $\sim$40 μm.

The matrix consisted primarily of $\sim$2–10 μm-sized grains of γ-TiAl (ordered $L1_0$ tetragonal structure) with small regions of α_2-Ti_3Al (ordered hexagonal

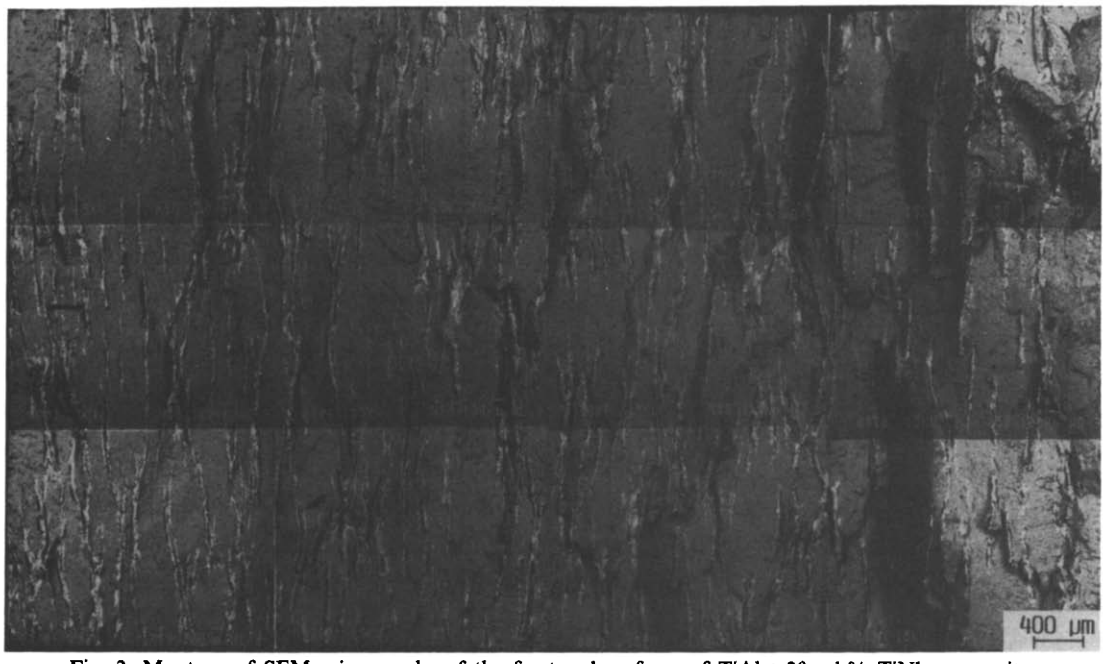

Fig. 3. Montage of SEM micrographs of the fractured surfaces of TiAl + 20 vol.% TiNb composite showing the distribution of ruptured ductile TiNb particles. Note the variations in particle thickness and the non-uniformity of their distribution.

DO_{19} structure). Yield and ultimate strengths for unreinforced γ-TiAl range between 400 and 500 MPa at room temperature with a tensile elongation of $\sim 1.8\%$ [3, 4]. While the yield strength (σ_0) of the TiNb phase is about 430 MPa, this solid-solution hardened Ti–Nb alloy does not post-yield harden (strain-hardening exponent, $n \sim 0$). Thus, deformation in the TiNb phase is highly localized and the measured fracture strains strongly depend on specimen geometry and gauge length. Niobium, on the other hand, has a lower yield strength of about 140 MPa, but strain hardens extensively with an initial exponent of $n \sim 0.3$, reaching an ultimate strength (σ_u) of 250 MPa before failing at a nominal fracture strain of ~ 0.45 [9].

2.2. *Interface characteristics*

Thermomechanical processing at high temperatures caused interfacial reactions between the γ-TiAl matrix and TiNb and Nb reinforcements (Fig. 4) [10, 17]. The ~ 5–$10\ \mu$m thick reaction product layer between TiNb and TiAl was composed of α_2 (~ 3–$5\ \mu$m) separated by a sharp boundary from a mixed region (~ 2–$5\ \mu$m) of α_2 and B_2 (ordered), and possibly some ω ($B8_2$) phase. Transmission-electron microscope (TEM) observations in Fig. 4(e) also indicated the presence of dislocations in ductile α_2 grains within the TiNb/TiAl reaction layer interface. The corresponding Nb/TiAl interface consisted of a ~ 1–$2\ \mu$m brittle σ (D_8) region and thinner layers of T_2 (Ti–44Al–11Nb at.%) and δ (Nb_3Al–A15 structure) adjacent to TiAl and Nb phases, respectively. In addition, microcracks were observed in the relatively brittle (dislocation- and twin-free) σ grains [Fig. 4(b)]. The reaction-layer phases are critical in mediating the interface toughness, debonding characteristics and resultant constrained-deformation behavior of the reinforcing phase; results are summarized in Table 2.

In the case of Nb/TiAl, the brittle σ reaction-layer phases result in a significant amount of debonding;

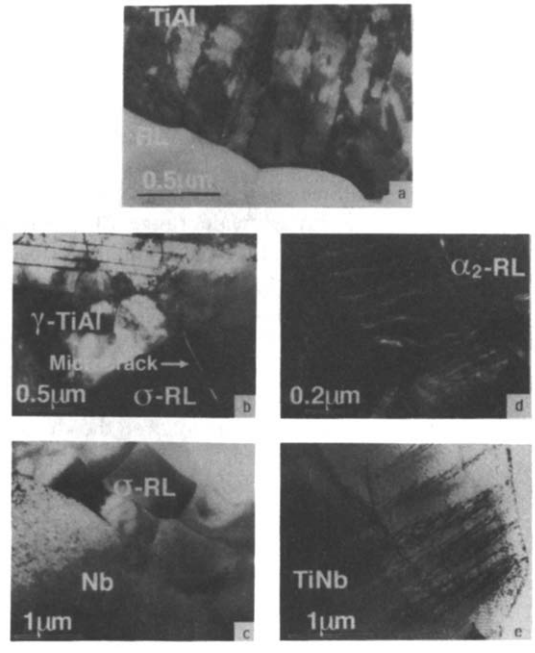

Fig. 4. Transmission electron microscope images of the reaction-layer (RL) interface characteristics between (a–c) Nb and γ-TiAl, and (d,e) β-TiNb and γ-TiAl.

Table 2. Summary of interfacial properties between TiNb/TiAl and Nb/TiAl

Interface	Interface phase	Maximum stress σ_{max}/σ_0	Critical displacement u^*/t	Debond length l_d/t	Work of rupture χ	Interfacial fracture energy $\Gamma_i(J/m^2)$
TiNb/γ-TiAl	α_2	2.2 ± 0.3	0.7 ± 0.2	<0.2	1.1 ± 0.2	>330
Nb/γ-TiAl	σ	1.8 ± 0.2	1.1 ± 0.3	1.0 ± 0.3	1.3 ± 0.3	~ 45

the interfacial toughness is estimated to be about 45 J/m^2 [9]. Typical debond length to particle thickness ratios (l_d/t) were roughly unity compared to values of about 4 reported for laminate foils [9]. This difference is probably due to the irregular shape and smaller thickness of the particles in the composite. However, in either case, the effect of matrix constraint on $\sigma(u)$ is minimal and the peak stress (σ_{max}) and normalized failure displacement (u^*/t) are approximately equivalent to the corresponding ultimate tensile strength and total elongation strains measured in geometrically-similar tensile tests; values of σ_{max}/σ_0 and u^*/t for the Nb particles are ~ 1.8 and 2.2, respectively.

In contrast, only minimal particle debonding ($l_d/t < 0.2$) was observed for the TiNb/TiAl composites compared to values of 0.75 ± 0.25 observed in sandwich tests [9], again the variation being attributable to the particle thickness and shape. Debond cracking occurred in the γ-TiAl matrix or γ/α_2 interface, suggesting a reaction-layer toughness in excess of ~ 330 J/m^2. Particle constraint factors cannot be measured directly but are expected to be at least comparable to values between 2 and 2.5 measured in sandwich tests; in fact, the constraint may be even higher due to the minimal debonding. The critical crack-opening displacements, u^*/t, were ~ 0.7.

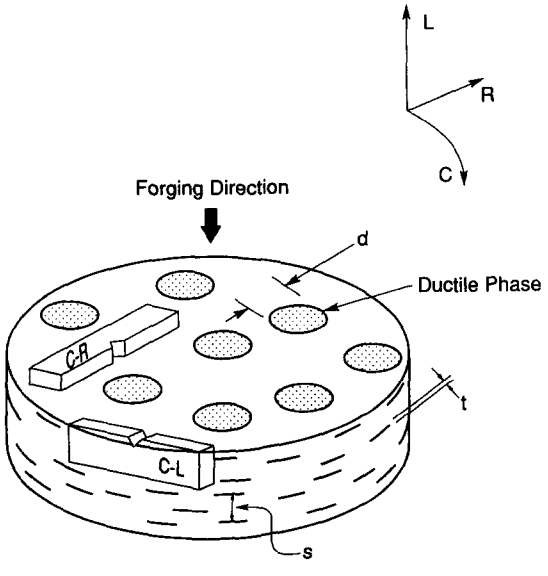

Fig. 5. Nomenclature for specimen and reinforcement orientations in the composite forging, namely C–R and C–L; L, C and R refer to the forging, circumferential and radial directions, respectively. C–R and C–L are also referred to as the *Edge* and *Face* orientations, respectively.

2.3. *Fracture toughness testing*

The fracture toughness behavior of TiNb/TiAl and Nb/TiAl composites was characterized in terms of $K_r(\Delta a)$ resistance curves, i.e. toughness as a function of crack extension. Specimens were fabricated by electro-discharge machining in two different orientations relative to the forging direction, namely, C–R and C–L (Fig. 5). The crack intersects the *edges* of the pancake-shaped particles in the C–R orientation; in the C–L configuration the crack intersects the *faces* of the pancakes [11]. Hence, C–R and C–L are subsequently referred to as the edge and face orientations, respectively. Tests were conducted using ~ 5 mm thick and 12.7 to 15.2 mm wide, pre-cracked, single-edge notch bend SE(B), TiNb/TiAl composite specimens, with a span-to-width ratio of about 3:1, loaded in three-point bending; the Nb/TiAl samples were 2.5 mm thick and 7.5 mm wide. To facilitate a direct comparison of the extrinsic toughening behavior in the various composites, a set of 7.5 mm wide TiNb/TiAl specimens were also tested.

Pre-cracking was achieved by initiating stable crack growth from the electro-discharge machined chevron notch by slow monotonic loading, under displacement control, using a servo-hydraulic testing machine. Subsequently, a major portion of the pre-crack bridging zone was removed by grinding the crack wake to within $\sim 50\ \mu$m behind the crack front. The final pre-crack depth to specimen width ratio (a_0/W) varied from about 0.3–0.5 for the various test samples.

R-curve tests were carried out by monotonically loading the pre-cracked samples under displacement control in laboratory air (~ 22°C, $\sim 45\%$ relative humidity) until crack extension was initiated. Crack lengths and crack/particle interactions were monitored using a high-resolution optical video camera system. In general, crack initiation was followed by a load drop and crack arrest after a small yet rapid uncontrolled jump. Automated detection of these load drops or direct observation of crack extension was used to trigger additional unloading, by about 15%, to further stabilize cracking. After measuring the new crack length (and recording other relevant observations), loads were again increased until the next initiation event. Applied load and crack-length measurements were used to calculate the initiation/re-initiation stress intensities (K_r) according to ASTM Standard E-399 [18]. The complete resistance curve was evaluated up to a/W ratios >0.8 by carrying out a large number of interrupted initiation/arrest (loading/unloading) cycles.

It is important to emphasize that small-scale bridging conditions, stipulated by the model in equation (1), are seldom met in practice under monotonic loading. For the TiNb/TiAl and Nb/TiAl composites studied in this work, monotonic bridging-zone lengths are often comparable to specimen and crack size dimensions, i.e. large-scale bridging conditions are prevalent; specimen widths in excess of 500 mm would be needed in some cases to fulfill small-scale bridging requirements. Crack-growth behavior under large-scale bridging is a function of the entire $\sigma(u)$ function as well as K_i and E' [11]; moreover, the extrinsic, large-scale bridging toughness can be significantly greater than K_{SSB} and is sensitive to test specimen size and geometry. Accordingly, R-curve measurements in this study must be considered as *extrinsic* and explicitly depend both on specimen width and initial a_0/W. While repeated tests demonstrated that results were reproducible, reinforcement heterogeneity and specimen-to-specimen differences in W and a_0/W can complicate direct comparison of $K_r(\Delta a)$ curves for the various composite architectures. Effects of these variations were mitigated, whenever possible, by comparing results for the most similar and representative test specimens and excluding data for a/W values greater than 0.8. In addition, corrections to experimental crack-growth data were made, where necessary, to account for large-scale bridging. Small-scale bridging conditions may, however, be common under cyclic loading because of the short bridging zones.

2.4. Fatigue-crack propagation testing

Cyclic crack-growth behavior in TiNb/TiAl composites under tension-tension loading was examined primarily with 25 mm-wide, 2.5 mm-thick, compact tension C(T) specimens in the edge (C–R) orientation; approximately 1-mm thick C(T) samples were used to characterize behavior in pure TiNb. Due to limitations in the available material, corresponding properties in the face (C-L) orientation of TiNb/TiAl composites and unreinforced γ-TiAl were determined using 15 mm-wide, 2.5 mm thick SE(B) samples (span $\sim$60 mm) loaded in four-point bending. Behavior in Nb/TiAl (face orientation) was examined using 2.5 mm-thick and 7.5 mm-wide samples under identical loading conditions. All specimens were fabricated with a wedge-shaped (semi-chevron) starter notch to facilitate fatigue pre-cracking, which was performed under alternating tensile loads prior to testing.

Experiments were performed in laboratory air ($\sim$22°C, $\sim$45% relative humidity) on computer-controlled servo-hydraulic testing machines operating under stress-intensity control. This was achieved by continuously monitoring the crack length, to a resolution better than $\pm 5\,\mu$m, using thin metallic foils bonded to the specimen surface, similar to techniques used for fatigue testing of ceramics [19, 20]. Unless otherwise stated, cyclic loads were applied at a constant nominal load ratio, $R\,(=K_{min}/K_{max})$, of 0.1 and a frequency of 50 Hz (sine wave); however, additional tests at R ratios of 0.5 and 0.7 were carried out on selected composites. To characterize the crack-growth rate behavior at different stress intensities, the applied stress-intensity range, $\Delta K\,(=K_{max}-K_{min})$, was gradually increased and/or decreased using exponential load-shedding schemes (variable ΔK at constant R), with the K-gradient set to $\pm 0.1\ \text{mm}^{-1}$ [21]. Using such procedures, crack-growth rates per cycle (da/dN) ranging between 10^{-6} and 10^{-12} m/cycle were obtained; the stress-intensity range corresponding to the slowest growth rate, $da/dN \leqslant 10^{-12}$ m/cycle, is operationally defined as the fatigue threshold, ΔK_{TH}, below which no appreciable crack extension is observed for specific cyclic loading conditions. Tests on Nb- and TiNb-reinforced TiAl composites were terminated under increasing-ΔK conditions, at ΔK levels marking the acceleration in crack-growth rates to very high values; for monolithic γ-TiAl, the tests ended when the specimen fractured. Cyclic crack-growth data are presented in terms of the crack-growth rate per cycle, da/dN, as a function of the applied stress-intensity range, ΔK.

Premature contact between the cracked surfaces above the minimum load (crack closure) was monitored using strain gauges mounted on the back face of the specimens; the closure stress intensity, K_{cl}, was specified by the load at the first deviation from linearity on the unloading compliance curve, reflecting initial contact between the two surfaces. Where K_{cl} exceeds K_{min}, the *local* (near-tip) stress-intensity range can be computed as $\Delta K_{eff} = K_{max} - K_{cl}$. The extent of bridging by ductile particles under cyclic loading was estimated by comparing the crack length (of a bridged crack) estimated from back-face strain compliance with equivalent values (for an unbridged crack) measured using bonded metal-foil gauges; procedures are described in Ref. [22]. These global estimates were supplemented by *in situ* observations of crack/particle interactions on the specimen surface, using a high-resolution optical telescope.

2.5. Fractography

Profiles of crack paths in the plane of loading and crack fronts across the specimen thickness were examined by taking metallographic sections parallel and normal to the crack growth direction, respectively. These sections and all fracture surfaces were imaged using optical and scanning electron microscopy (SEM). In addition, crack-reinforcement interactions and specific fracture mechanisms were examined by SEM by periodically interrupting tests (cyclic loading) or by using an *in situ* loading stage in the microscope (monotonic loading).

3. RESULTS AND DISCUSSION

3.1. Fracture toughness properties

The basic processes leading to toughening under monotonic loading in the TiAl composites examined

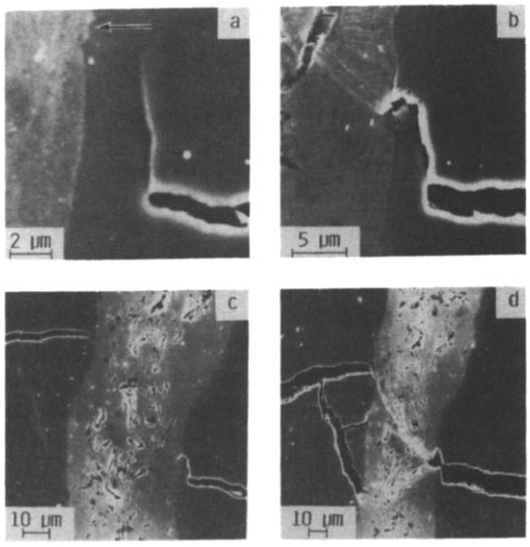

Fig. 6. Summary of crack/reinforcement interactions in TiNb/TiAl composites under monotonic loading, showing (a) crack arrest at the interface with minimal debonding between TiAl and the reaction layer, (b) crack-tip blunting at the TiNb particle, (c) renucleation of the crack in front of the particle leading to crack bridging, and (d) large-scale plastic deformation in the TiNb particle leading to final rupture. Images were obtained using a SEM with an *in situ* loading stage; arrow indicates the general direction of crack growth.

are illustrated in Figs 6 and 7. Specifically, Fig. 6 shows a typical sequence of events as the crack intersects a ductile TiNb particle in the composite: (a) crack arrest at the ductile α_2 layer; (b) penetration of the reaction layer and initiation of plastic deformation in the particle; (c) renucleation in the matrix ahead of the particle; and (d) large-scale deformation along intense slip bands prior to particle rupture. Note that the TiNb particles do not decohere from the matrix during crack extension but exhibit limited debond cracking along the γ/α_2 interface, as seen in Fig. 6(a) and 6(b), similar to observations made on sandwiched-composite tests [9]. The bridging zones, i.e. the length scales over which TiNb reinforcements remain intact in the crack wake, are on the order of several millimeters (Table 3).

The resulting composite fracture surfaces in Fig. 7 show minimal secondary cracking at the interface. The constituent phases exhibit similar fractographic

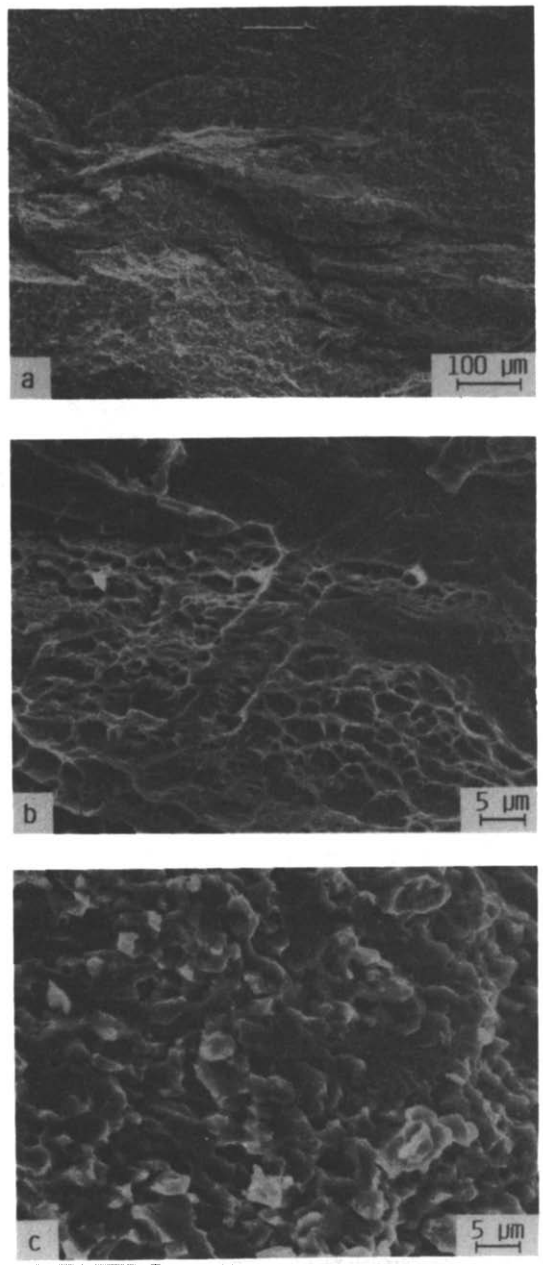

Fig. 7. Fractography of fracture surfaces in TiNb/TiAl composites under monotonic loading, (a–c) at various magnifications, showing (b) transgranular cleavage failures in γ-TiAl, and (c) dimpled rupture in the ductile TiNb phase. Arrow indicates the general direction of crack growth.

Table 3. Summary of monotonic crack-growth data in γ-TiAl composites

Reinforcement	Volume fraction f	Particle thickness t (μm)	Initiation toughness K_i (MPa$\sqrt{}$m) Edge	Face	R-Curve slope dK_r/da (MPa$\sqrt{}$m/mm) Edge	Face	Steady-state toughness K_{SSB} (MPa$\sqrt{}$m)	Steady-state bridge length L_{SSB} (mm)
TiNb	0.05	40	11.3	12.7	2.1	2.5 (1.9)[a]	18.3	38.8
TiNb	0.1	40	18.6	15.7	2.5	3.3 (2.9)[a]	24.7	22.3
TiNb	0.2	40	17.3	19.0	4.2	5.0	32.6	13.7
TiNb	0.2	20	18.9	18.4	2.3	2.4 (2.2)[a]	26.6	5.3
TiNb[b]	0.2	40	17.5	19.1	12.4	9.6	32.6	13.7
Nb[b]	0.2	40	12.2	13.8	6.9	5.5	21.2	57.5

[a]Values in parenthesis are corrected to 15.2 mm width.
[b]7.5 mm-wide specimens.

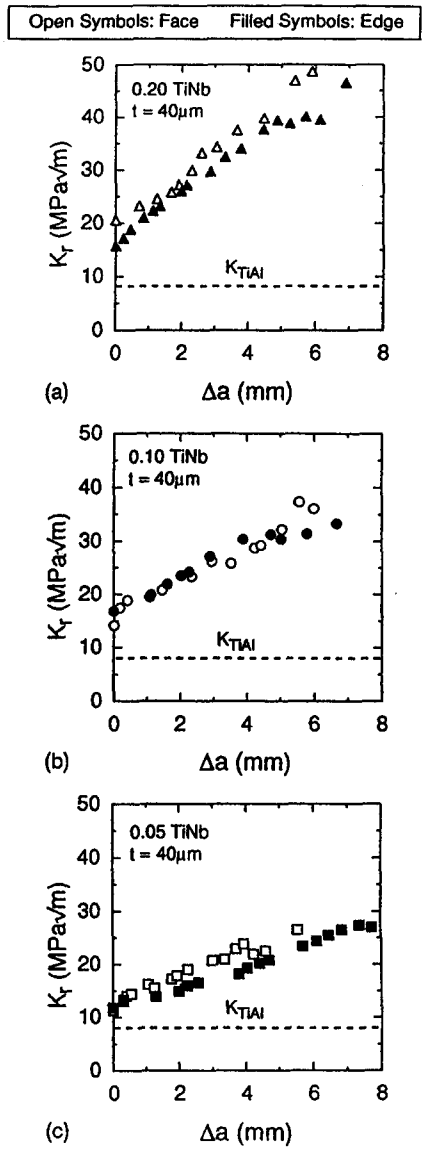

Fig. 8. Resistance curves characterizing the crack-growth behavior in TiNb/TiAl composites under monotonic loading, as a function of the volume fraction, (a) 20, (b) 10 and (c) 5 vol.% of TiNb phase (thickness, $t = 40\,\mu$m), in the edge (or C–R, denoted by open symbols) and face (or C–L, denoted by filled symbols) orientations. Dashed line K_{TiAl} represents the toughness of pure γ-TiAl.

features in composite and monolithic form; the ductile TiNb particles fail by a transgranular, microvoid nucleation and coalescence mechanism, as evidenced by the dimpled surfaces in Fig. 7(b). Fractures in γ-TiAl are predictably brittle, characterized by transgranular cleavage with small regions showing intergranular failure [Fig. 7(c)]. The distribution of ruptured ductile TiNb particles dispersed over the brittle TiAl fracture surface is illustrated in Fig. 3.

Effects of these crack-extension processes on resistance-curve behavior as a function of the ductile-reinforcement characteristics are summarized in Figs 8 and 9; estimates of the crack-initiation toughness, K_i, and R-curve slope, dK_r/da, values based on linear

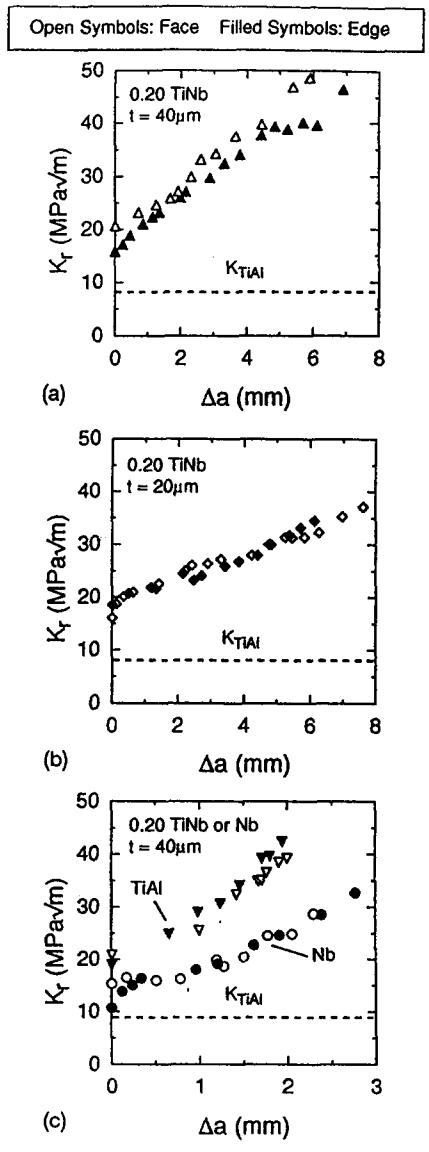

Fig. 9. Influence of (a,b) reinforcement thickness, t, of 20 μm vs 40 μm, and (c) reinforcement type, TiNb vs Nb, on the monotonic crack-growth resistance of γ-TiAl composites, for a volume fraction, $f = 0.2$, in the edge (open symbols) and face (filled symbols) orientations. Note that results presented in Fig. 9(c) were obtained using 7.5 mm-wide specimens (under large-scale bridging), both for TiNb/TiAl and Nb/TiAl composites, to enable a direct comparison; all other data presented are for 15 mm-wide samples. Dashed line represents the toughness of pure γ-TiAl, K_{TiAl}.

†Note that specimens in the face orientation with TiNb volume fractions of 0.05 and 0.10 were 12.7 mm-wide compared to the typical width of 15.2 mm. While the crack-initiation toughness would not be influenced by such size differences, K_r increases more rapidly with crack advance in smaller test specimens. For example, large-scale bridging calculations indicate that at crack extensions of 7 mm, the smaller specimen size increases the extrinsic toughness by ~25% and ~13% for the 5 and 10 vol.% TiNb-reinforced γ-TiAl composites, respectively.

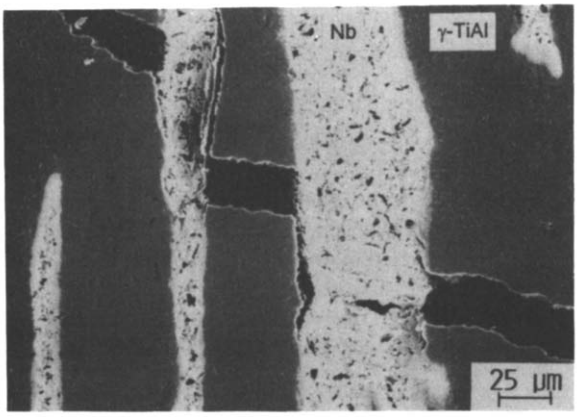

Fig. 10. SEM micrograph of fracture path morphologies in Nb/TiAl composites under monotonic loading. Note the extensive debonding at the interface compared to TiNb/TiAl composites.

least-square fits to the experimental data are listed in Table 3. Despite the influence of specimen size on the measured fracture properties†, it is clear that both crack-initiation toughness and crack-growth toughness, i.e. the slope of the resistance curve, increase with ductile-phase content for the 40 μm-thick TiNb reinforcements [Fig. 8(a–c)]. In comparison, reinforcement orientation has a minimal effect on ductile-phase toughening at lower volume fractions, particularly after specimen-size variations are considered. The toughness is marginally superior in the face orientation, compared to the edge, but only for TiAl composites reinforced with 20 vol.% TiNb.

The reduction in reinforcement thickness from $\sim$40 to 20 μm at a volume fraction of 0.2 decreases the slope of the resistance curve, but does not appear to have a large effect on the initiation toughness [Fig. 9(a, b)]. The effectiveness of Nb vs TiNb ductile reinforcements in enhancing the monotonic fracture resistance of γ-TiAl composites, compared in Fig. 9(c), illustrates the significance of *effective* particle strength on toughness as mediated by the combination of yield stress, constraint (for TiNb) and strain hardening (for Nb). Specifically, the Nb particles in Nb/TiAl composites readily delaminate from the matrix during crack advance (Fig. 10) and relax constraint (or reduce the degree of triaxiality) during fracture compared to the highly constrained failure of TiNb ligaments in TiNb/TiAl composites (Fig. 6). Consequently, the higher (constrained) maximum effective strength of the TiNb reinforcements ($\sim$950 MPa) yield a significantly higher crack-initiation toughness and a steeper resistance curve compared to Nb additions (unconstrained, effective strength of Nb $\sim$250 MPa). The larger critical opening displacement in Nb ($u^* \sim 1.1t$) vs TiNb ($u^* \sim 0.7t$) appears to have no effect on the initiation toughness and relatively little effect on crack-growth toughness in these small samples. Furthermore, little effect of orientation on toughness is noted for either reinforcement.

The effects of reinforcement volume fraction (f) and thickness (t) on the apparent crack-initiation and crack-growth toughness values are more clearly shown in Fig. 11(a–c) [the small symbols in Fig. 11(a)

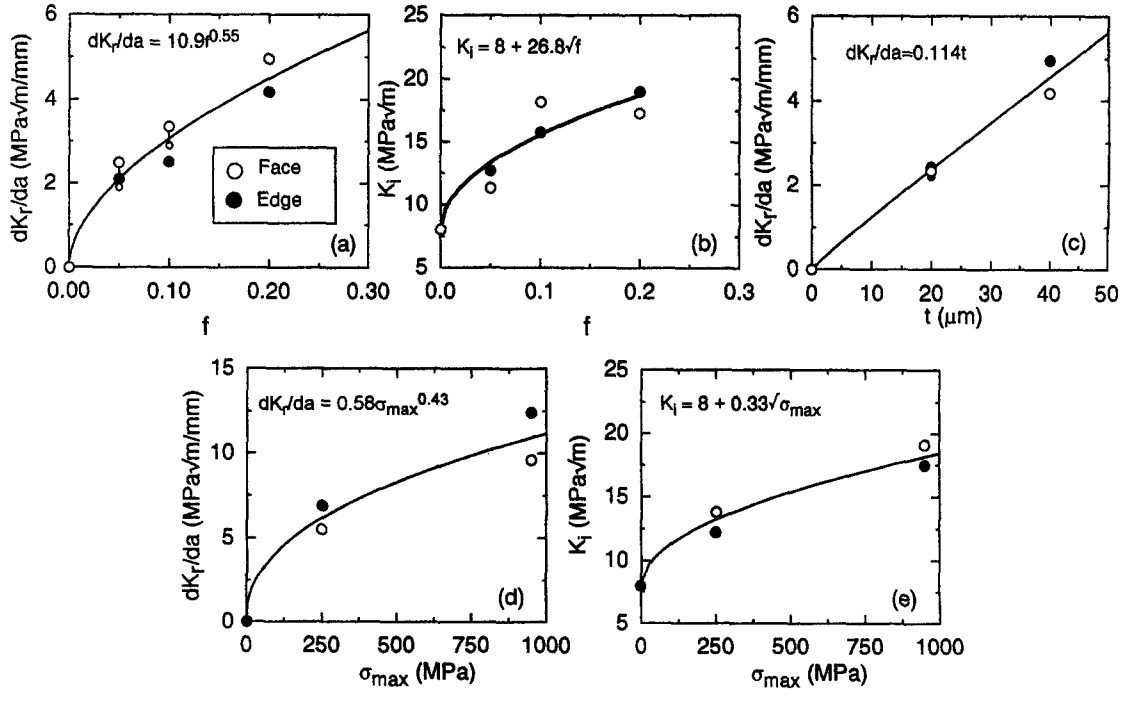

Fig. 11. Variations in crack-initiation toughness, K_i, and crack-growth toughness, dK_r/da, with (a,b) volume fraction f, of reinforcement phase, (c) particle thickness, t, and (d,e) reinforcement strength, σ_{max}, for both Nb/TiAl and TiNb/TiAl composites.

represent the estimated size corrections to a common specimen width of 15.2 mm]. With respect to volume fraction of TiNb, f_{TiNb}, [Fig. 11(a, b)] power-law fits yield

$$\frac{dK_r}{da} = 10.9(f_{TiNb})^{0.55}$$

$$K_i = 8 + 26.8(f_{TiNb})^{0.5}. \quad (3)$$

The corresponding fit of dK_r/da to the TiNb particle thickness, t_{TiNb}, yields a linear dependence [Fig. 11(c)]. Particle thickness has little effect on crack-initiation toughness; hence, a plot of these data is not shown. Figure 11(d) and (e) plot the apparent crack-initiation toughness values and resistance-curve slopes vs the effective maximum reinforcement strength, yielding power-law fits

$$\frac{dK_r}{da} = 0.58(\sigma_{max})^{0.43} \quad (4)$$

$$K_i = 8 + 0.33(\sigma_{max})^{0.5}. \quad (5)$$

The extrinsic toughening behavior measured in this study cannot be analyzed using the intrinsic, steady-state, small-scale bridging model represented by equation (1). Nevertheless, the experimental trends are *qualitatively* consistent with predictions that toughness increases with the square root of the reinforcement volume fraction and strength. The linear dependence of toughness on particle thickness is not predicted by equation (1). The particle thickness effect on crack-growth toughness (dK_r/da) is probably a consequence of the combination of a higher effective strength (particularly in the initial portion of the R-curve) and longer extrinsic bridge length (particularly at large a/W) for the large-scale bridging conditions experienced in these tests.

One puzzling result, however, is the absence of an effect of particle thickness on the apparent initiation toughness. Recall that the elevation of K_i above the K_{Ic} value for γ-TiAl matrix is attributed to a combination of crack trapping, deflection, and renucleation mechanisms along with the presence of a small ($\sim 50\ \mu m$) residual crack-bridging zone. While crack deflection contributions are not believed to be significant, the toughening increment associated with renucleation and residual bridging effects would be expected to scale roughly with the square root of the reinforcement thickness [11, 23]. This suggests that crack trapping (pinning by ductile phases, as in the case of a tunnel crack) effects in the edge orientation may be comparable to toughening contributions from crack-renucleation mechanisms in the face orientation. More research is needed to resolve the effect of particle thickness and orientation on the apparent crack-initiation toughness.

A more rigorous analysis of these data must take into account the effects of large-scale bridging, by calculating self-consistent solutions to the crack-opening profile, $u(x)$, the distribution of tractions in the crack wake, $\sigma(x)$, and the stress-displacement function of the composite, $\sigma(u)$, where x is the distance behind from the crack tip; details are presented elsewhere [11]. Using this model, the intrinsic steady-state toughness, K_{SSB}, and steady-state bridging length, L_{SSB}, were estimated by computing the $K_r(\Delta a)$ curves up to steady-state in a very large specimen. The calculations assumed nominal reinforcement parameters given in Table 2; K_t and E' are approximated by the initiation toughness, K_i, and the nominal plane-strain elastic modulus of TiAl (193 GPa). The stress-displacement function for the composite is of the form

$$\sigma(u) = \sigma_{max}(u/u_p) \text{ for } u \leqslant u_p \quad (6a)$$

$$\sigma(u) = \sigma_{max}[1 - (u/u'^*)^{0.5}] \text{ for } u > u_p \quad (6b)$$

where, u_p is the displacement at peak stress (taken as $2\ \mu m$), and u'^* is taken as twice the *average* critical particle displacement or the corresponding value measured in sandwich tests. This formulation of $\sigma(u)$ is a modification to the nearly saw-toothed stress-displacement functions measured in the sandwich tests in order to account approximately for the *distribution* of particle thicknesses in the actual composite. Results from these calculations, summarized in Table 3, also indicate that significant intrinsic toughening can be achieved in γ-TiAl composites even under small-scale bridging conditions. Also note the remarkably long steady-state bridging lengths under small-scale bridging conditions.

Results on crack-growth resistance curves measured under monotonic loading can be summarized as follows. Even small volume fractions of ductile reinforcements produce marked toughening due (i) the formation of large bridging zones and (ii) crack trapping and renucleation mechanisms which mediate the critical crack-tip stress intensity. The slope of the R-curve increases with reinforcement volume fraction, strength and thickness; with the exception of particle thickness, similar trends are observed for crack-initiation toughness. Reinforcement orientation appears to have relatively little effect on the degree of toughening on these composites. Overall, the experimentally measured extrinsic toughening behavior is consistent with predictions of large-scale bridging models.

3.2. *Fatigue-crack propagation behavior*

Cyclic fatigue-crack growth results in the ductile-particle reinforced γ-TiAl composites, along with data for unreinforced γ-TiAl and β-TiNb constituent phases, are plotted in Figs 12–14; fatigue-threshold data and other crack-growth parameters are summarized in Table 4. As noted in previous studies on the TiNb/TiAl system [15, 16], under cyclic loading, cracks propagate subcritically at stress intensities of 4–12 $MPa\sqrt{m}$ for all γ-TiAl composite microstructures and specimen orientations, below the K_i values necessary to initiate and sustain cracking under monotonic loading (Table 3). Subcritical crack

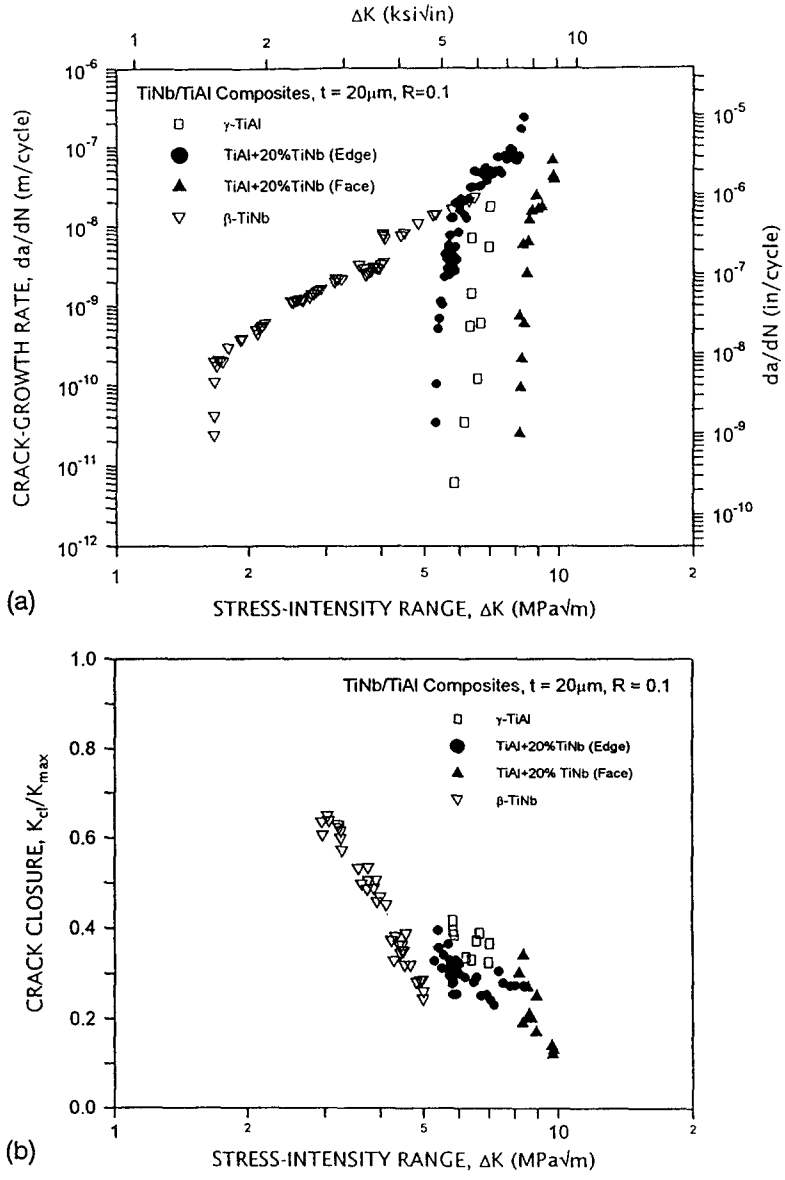

Fig. 12. (a) Cyclic crack propagation and (b) crack-closure behavior in a γ-TiAl + 20 vol.% β-TiNb ($t \sim 20\,\mu$m) composite, in the edge (C–R) and face (C–L) orientations, at $R = 0.1$, compared with the crack-growth properties of the constituent phases, monolithic γ-TiAl and β-TiNb.

propagation under cyclic loads must therefore be considered an important damage mode in the structural design and use of ductile-phase toughened brittle-matrix composites.

The general features on da/dN–ΔK curves for the composites resemble those seen for most metallic materials with a low-growth rate region (region I) at ΔK levels close to the fatigue threshold, where the rate of crack advance strongly depends on applied ΔK, followed by an intermediate or mid-growth rate region (region II) where this dependence is moderate. However, unlike behavior in metals, crack-growth behavior for the γ-TiAl composites in this mid-growth rate regime† is still very sensitive to the applied ΔK, especially at low volume fractions. In fact, when expressed in terms of the empirical Paris power-law relationship that is often used to describe fatigue crack-growth rate behavior in this region.

$$da/dN = C\Delta K^m \tag{7}$$

the exponent m ranges between 10 and 20 for the various composites, compared to values of ~2–4 that are typically reported for monolithic metallic materials; $m \sim 4.6$ for pure β-TiNb [Table 4, Fig. 12(a)]. In other words, the mid-growth rate (power-law) regime of cyclic crack growth is relatively small for ductile-phase toughened TiAl composites and virtually non-existent for unreinforced γ-TiAl ($m \sim 30$). At high ΔK levels approaching the

†Behavior in this region is characterized by curve fitting the da/dN data between 10^{-9} and 10^{-6} m/cycle.

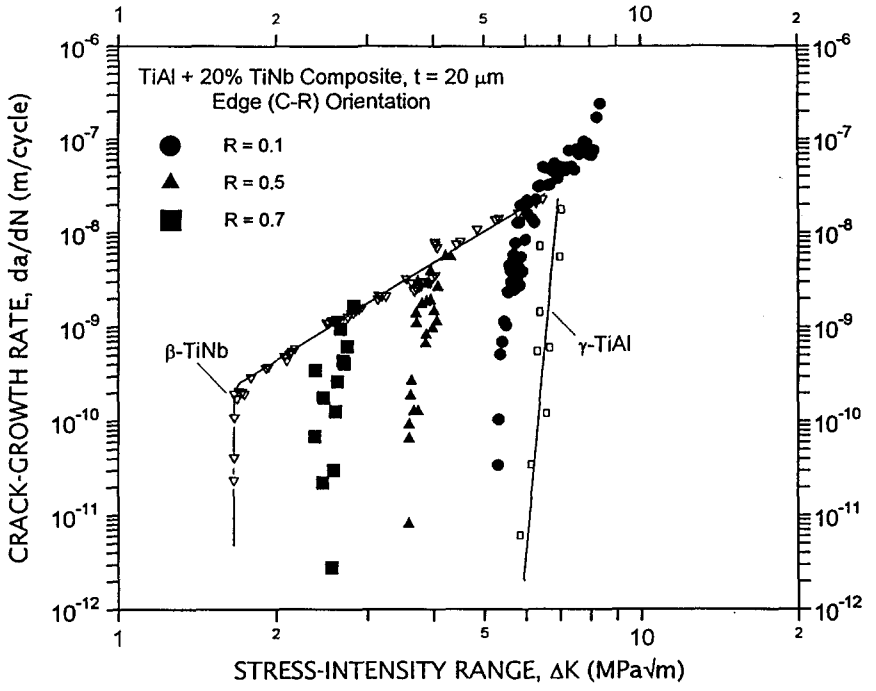

Fig. 13. Influence of load ratio, $R = 0.1$, 0.5 and 0.7, on the cyclic fatigue-crack growth behavior in a γ-TiAl composite reinforced with 20 vol.% ($t \sim 20\,\mu$m) TiNb particles in the edge (C–R) orientation.

initiation toughness, K_i (high-growth rate regime, region III), a rapid increase in crack-extension rates is seen for small changes in ΔK, similar to behavior near the fatigue threshold.†

3.2.1. Orientation effects for TiNb/TiAl composites. Figure 12(a) depicts the cyclic fatigue-crack growth data for the edge and face orientations in the γ-TiAl composite reinforced with 20 vol.% of $\sim 20\,\mu$m-thick TiNb particles. Specifically, in the edge orientation, region I fatigue-crack growth rates in the composite are faster than in unreinforced γ-TiAl and much slower than in pure β-TiNb. The near-threshold cyclic crack-growth behavior ($da/dN < 10^{-9}$ m/cycle) of the composite is essentially bounded by properties of the individual phases. In region II, growth rates in the edge-orientation of the composite are comparable to those measured in monolithic β-TiNb.

However, Fig. 12(a) also reveals that the crack velocities in the TiNb/TiAl composite for the face (C-L) orientation are slower than in γ-TiAl; in fact, the composite fatigue properties are superior to both unreinforced TiAl and TiNb. Thus, unlike the response under monotonic loading, the reinforcement orientation has a marked effect on cyclic crack-growth behavior. More importantly, these results clearly demonstrate that the incorporation of ductile reinforcements *can* also enhance the cyclic fatigue-crack propagation resistance of brittle γ-TiAl intermetallic alloys, in addition to improving their fracture toughness. However, the magnitude of improvement is relatively small, indicated by $\sim 2\,\text{MPa}\sqrt{\text{m}}$ shift in the entire da/dN–ΔK curve compared to the nearly five-fold increase in toughness seen under monotonic loads, and is seen only specific orientations i.e., where the crack periodically encounters the pancake faces of ductile particles. Similar reinforcement-orientation effects are also observed in other TiNb/TiAl composite microstructures [Fig. 14(b)].

Corresponding measurements of the extent of crack closure in the TiNb/γ-TiAl composites and their two unreinforced constituents are shown in Fig. 12(b) in terms of the closure stress intensity, K_{cl}, normalized by K_{max}, as a function of ΔK. The K_{cl}/K_{max} values in the edge orientation of composite are slightly lower compared to TiAl in the edge orientation suggesting faster growth rates due to increased ΔK_{eff} values locally at the crack tip; no such distinction is apparent in the face orientation. Although such variations are partly consistent with observed reinforcement-orientation effects on cyclic crack growth, closure effects do not appear to completely account for the differences in crack-growth rates between the composite and monolithic alloys. Specifically, at high ΔK levels where the influence of closure is reduced, cracks propagate faster in the edge-oriented composite than in pure γ-TiAl or β-TiNb [Fig. 14(a)]. As such, it seems more likely that cyclic crack-growth rate variations are principally

†It should be noted that fatigue-crack growth behavior in the high-ΔK regime (region III) has not been fully characterized in this study due to the rapid crack velocities inherent with test frequencies of 50 Hz used for cyclic loading, especially for brittle-matrix composites.

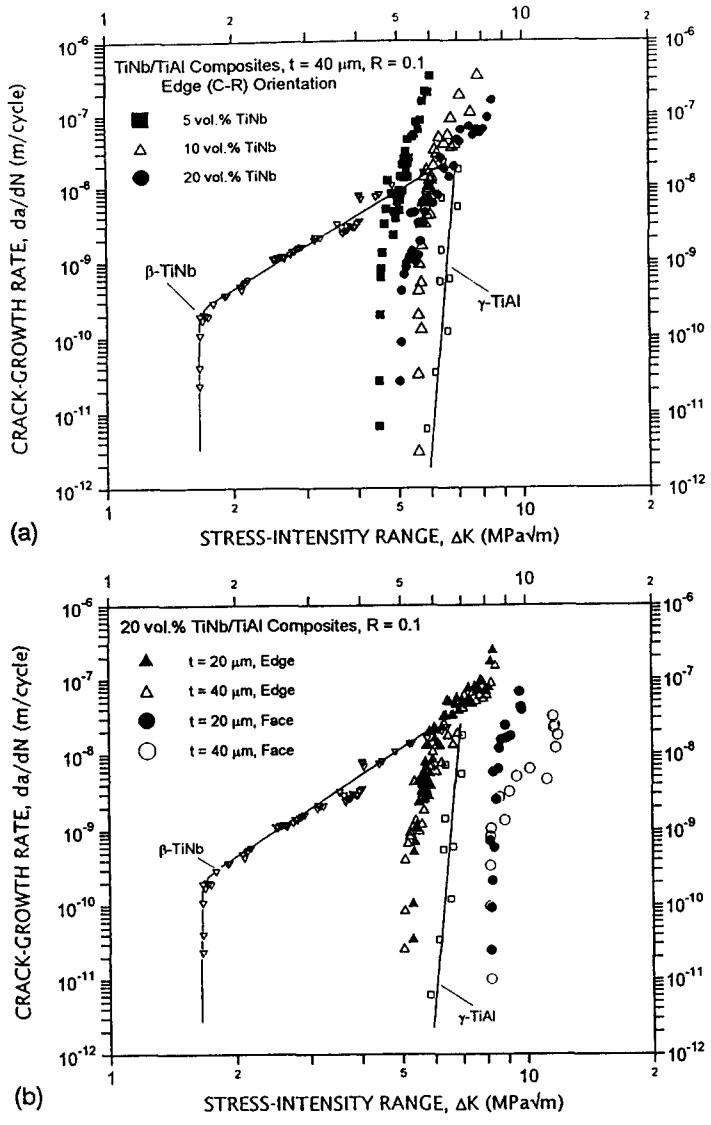

Fig. 14. Microstructural effects of (a) volume fraction ($t \sim 40\ \mu$m) and (b) particle thickness ($f \sim 0.2$) on the cyclic fatigue-crack propagation resistance of TiNb/TiAl composites in the edge (C–R) orientation, at $R = 0.1$.

attributable to differences in intrinsic mechanisms of cyclic crack advance in these microstructures.

3.2.2. Load ratio effects. The effect of load ratio ($R = K_{min}/K_{max}$) on cyclic crack-growth rates, in the 20 vol.% TiNb/γ-TiAl composite in the edge (C–R) orientation, is shown in Fig. 13. Compared to a baseline of $R = 0.1$, load ratios of 0.5 and 0.7 reduce the fatigue threshold stress-intensity values by about 27 and 51%, respectively. This phenomenon is consistent with behavior observed in many metallic materials [24], where increasing R accelerates crack-growth rates for a given ΔK, especially in the near-threshold and high-ΔK regions. Although the marked sensitivity to applied ΔK in the threshold regime is essentially unchanged, higher load ratios suppress the intermediate growth-rate regime (region II) separating the behavior at near-threshold and high stress intensities. The latter occurs at K_{max} of $\sim$8.5–9.3 MPa$\sqrt{m}$, slightly in excess of the matrix fracture toughness of $\sim$8 MPa$\sqrt{m}$, and is independent of the load ratio.

As noted above, premature crack closure is observed to occur in the composites at stress intensities above K_{min}, presumably from the wedging of fracture-surface asperities including any intrinsic bridging ligaments or broken remnants, e.g. at threshold, K_{cl} is $\sim 0.4\ K_{max}$. As a result, for load ratios below 0.4, such closure causes a net increase in K_{min} or a reduction in the driving force from the nominal (applied) value of ΔK to a local "near-tip" value ΔK_{eff}, thereby resulting in slower crack-growth rates. At high R, closure effects are minimal ($K_{min} > K_{cl}$) and the crack remains open during the entire loading cycle; accelerated crack-growth rates are thus to be expected. From these considerations, load ratio effects on cyclic crack growth in the composite are

Table 4. Summary of cyclic crack growth data in γ-TiAl composites

Material	Load ratio R	Threshold ΔK_{TH} (MPa$\sqrt{m}$)	Exponent[a] m	Constant[b] C
γ-TiAl	0.1	5.8	29.4	9.7×10^{-31}
β-TiNb	0.1	1.7	4.6	3.0×10^{-11}
Edge orientation				
γ-TiAl + 5% TiNb (40 μm)	0.1	4.5	17.6	5.3×10^{-18}
+ 10% TiNb (40 μm)	0.1	5.6	14.1	1.1×10^{-16}
+ 20% TiNb (40 μm)	0.1	5.0	9.6	2.0×10^{-13}
+ 20% TiNb (20 μm)	0.1	5.3	9.7	2.5×10^{-13}
	0.5	3.6	—	—
	0.7	2.6	—	—
Face orientation				
γ-TiAl + 20% TiNb (40 μm)	0.1	8.2	6.7	1.0×10^{-15}
+ 20% TiNb (20 μm)	0.1	8.2	14.8	1.1×10^{-22}
+ 20% Nb (40 μm)	0.1	10.1	8.7	1.0×10^{-18}

[a]For crack-growth rates between 10^{-9} and 10^{-6} m/cycle.
[b]Units: m/cycle (MPa$\sqrt{m}$)$^{-m}$

expected to be small for $R > 0.4$, since K_{cl} is at least $\sim 0.4\,K_{max}$. However, other factors are clearly relevant in view of the marked differences in behavior between $R = 0.5$ and 0.7, e.g. the rapid crack growth at K_{max} levels approaching the matrix K_{Ic} due to cleavage fracture of γ-TiAl [Fig. 7(c)], akin to the high-ΔK behavior controlled by static-mode fracture mechanisms seen in metallic alloys [24].

3.2.3. Crack–particle interactions. In contrast to behavior under monotonic loads (Fig. 6), crack-path morphologies in TiNb/γ-TiAl microstructures under cyclic loads reveal that there is minimal ductile-ligament bridging in the crack wake (Fig. 15). Crack paths in the plane of loading and crack fronts across the specimen thickness ($\sim 150\,\mu$m behind the crack tip) clearly indicate that the TiNb particles rapidly fail under cyclic loading without any sign of plastic deformation. In the edge (C–R) orientation, fatigue cracks traverse the ductile particles apparently without significant interaction [Fig. 15(a)]; crack blunting, crack renucleation and resultant in-plane bridging effects, which are so dominant under monotonic

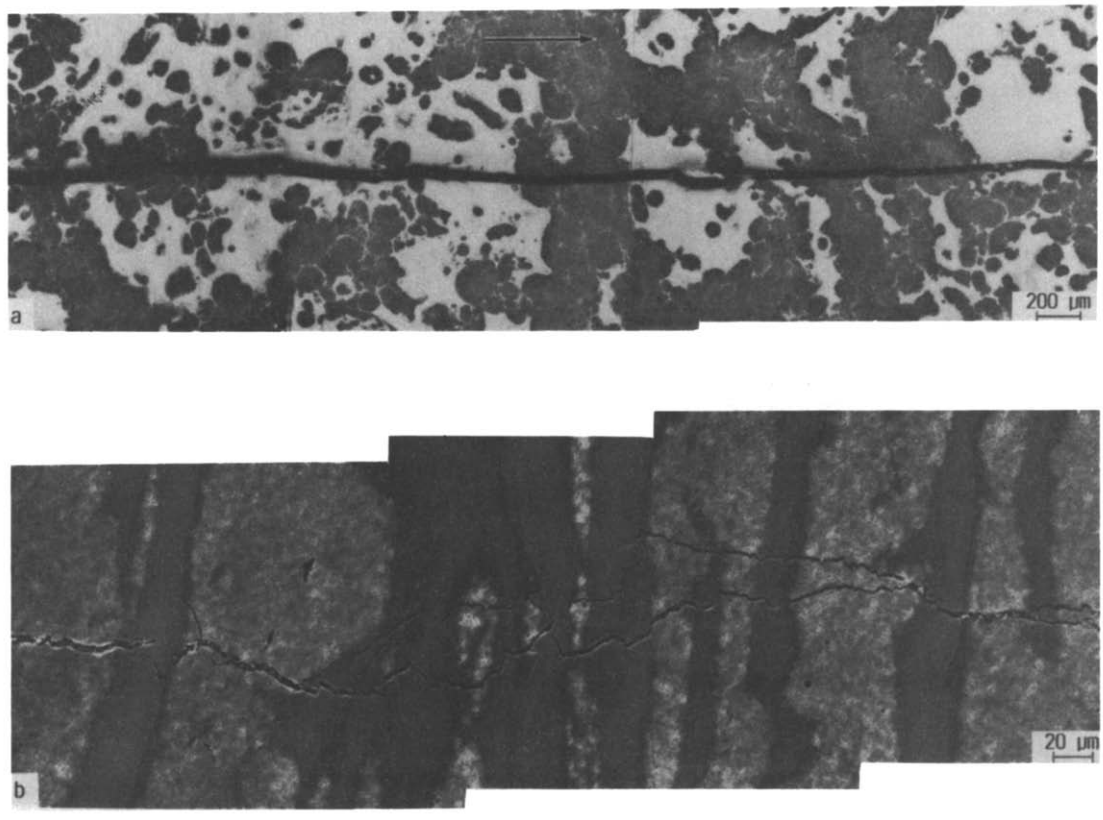

Fig. 15. SEM micrographs of crack-path morphologies in TiNb/γ-TiAl composites under cyclic loading in the (a) edge (C–R) and (b) face (C–L) orientations, taken at specimen mid-thickness location in the loading plane. Horizontal arrow indicates the crack-growth direction.

loads, are simply not observed. This conclusion was verified by *in situ* telescopic observations on the specimen surface, and also by quantitative estimates of the extent of crack bridging at various ΔK levels. Crack lengths, estimated from elastic-compliance measurements using strain gauges, were within $\pm 200\,\mu$m (<2%) of those measured using indirect d.c. potential methods, indicating that crack-bridging effects in fatigue are relatively insignificant. No discernible differences in crack paths were noted at the various load ratios.

Although cracking is still continuous through the matrix and ductile phases in the face (C–L) orientation, as shown in Fig. 15(b), there is indication of crack branching, deflection, multiple cracking in the matrix and coplanar bridging (associated with a non-planar and discontinuous crack front across the specimen thickness because of overlapping cracks on different planes), consistent with the improved crack-growth resistance in this orientation. Crack renucleation in the matrix ahead of the TiNb particle under cyclic loading is observed at ΔK levels of $\sim$9–10 MPa$\sqrt{\text{m}}$; however, due to the rapid fatigue fracture of the TiNb particle, the effective range of crack/particle interactions is limited to a few hundred microns or less (cyclic bridging zone $\sim$ particle thickness); equivalent dimensions under monotonic loading are on the order of several millimeters (Table 3). In fact, even in the face orientation, the TiNb particles show minimal evidence of plastic stretching.

Corresponding fracture-surface morphologies are shown in Fig. 16. Unlike the microvoid coalescence seen under monotonic loading (Fig. 7), the TiNb phase fails by transgranular shear under cyclic loading in both the composite and monolithic form [Fig. 16(b)]; features resemble fatigue failures in coherent-particle hardened alloys that deform by planar slip [25]. Likewise, the γ-TiAl matrix also shows intrinsic fatigue damage, evidenced by the parallel slip markings in Fig. 16(c), in addition to the transgranular and intergranular cleavage modes of failure [Fig. 16(c)].

From these observations and other studies [15, 16] it may be inferred that the lack of toughening from crack-bridging mechanisms under cyclic loads is the principal reason for subcritical crack-growth effects in TiNb/TiAl composites at ΔK levels below their crack-initiation toughness values. Such enhanced crack growth results from fatigue-induced failure of the ductile particles before the crack can establish a bridging zone, which is already limited under cyclic loading because of the relatively small crack-opening displacements associated with the lower stress intensities.

The sources for reinforcement-orientation effects on cyclic crack growth are not altogether clear. Potential explanations include: (i) fatigue failure of the reinforcements in the edge orientation in fewer cycles, since the opening along the crack flanks and resultant plastic displacements would be larger than corresponding crack-tip opening displacements in the face orientation; (ii) restriction of crack deflection, branching and coplanar bridging effects in the edge orientation by the reinforcement; and (iii) differences in the phase angle of any local debond cracks.

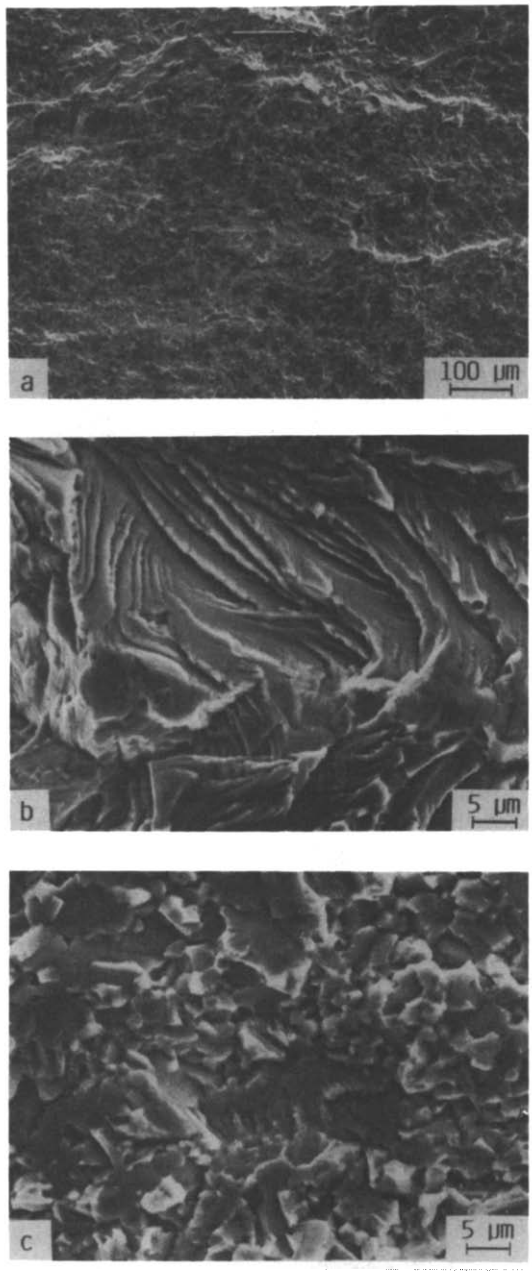

Fig. 16. (a–c) SEM images of fracture surfaces in TiNb/γ-TiAl composites under cyclic loading at various magnification levels. Micrographs (b) and (c) illustrate the cracking features in β-TiNb and γ-TiAl regions of the composite. Horizontal arrow indicates the general direction of crack growth.

3.2.4. Reinforcement size and volume fraction effects. The influence of TiNb reinforcement volume fractions, ranging between 0.05–0.2 ($\sim$40 μm-thick), on fatigue-crack growth behavior of TiNb/TiAl composites in the edge orientation, is illustrated in

Fig. 14(a). While fatigue thresholds for all composites fall below the value for monolithic γ-TiAl, there appears to be no consistent effect of f_{TiNb} on the fatigue threshold; ΔK_{TH} values range between $\sim 4.5\ MPa\sqrt{m}$ ($f_{TiNb} \sim 0.05$) and $\sim 5.6\ MPa\sqrt{m}$ ($f_{TiNb} \sim 0.1$).

However, the slope of da/dN-ΔK curves (measured as the exponent, m) in the intermediate growth-rate region is found to decrease consistently with increasing ductile-phase content (Table 4); the ΔK interval for region II and the maximum ΔK marking the onset of region III show a corresponding decrease. In effect, intermediate crack-growth rates in the composites, at a given ΔK, are lowered by increasing the reinforcement volume fraction. More notably, crack-growth rates in the composites with 10 vol.% TiNb, and particularly 5 vol.% TiNb, are significantly *higher* than those found in either unreinforced TiNb or TiAl. These interesting, albeit puzzling, effects could be associated with the competing role of residual stresses or crack-closure effects (which increase ΔK_{tip}) vs limited crack bridging/trapping (which reduces ΔK_{tip}); with increasing f_{TiNb}, crack bridging/trapping effects may become dominant.

Reinforcement thickness has a minimal effect on cyclic crack-growth behavior in the edge (C–R) orientation, for samples containing 20 vol.% TiNb [Fig. 14(b)]. However, increasing TiNb particle thickness from ~ 20 to 40 μm is found to retard crack advance in the face (C–L) orientation, especially for ΔK levels in the mid-growth rate regime, above $\sim 9\ MPa\sqrt{m}$. Toughening mechanisms associated with crack renucleation in the matrix ahead of the ductile particle, which scale with particle thickness [11, 23], are believed to account for the improved fatigue resistance of coarse microstructures. Once again, note that reinforcement-orientation effects are prominent under cyclic loading, with face-oriented composites exhibiting better crack-growth resistance over γ-TiAl and β-TiNb.

3.2.5. TiNb vs Nb reinforcements. Figure 17 compares the fatigue-crack growth properties of γ-TiAl reinforced with 20 vol.% ($\sim 40\ \mu$m thick) Nb particles in face (C–L) orientation to corresponding behavior in the TiNb/TiAl, both in the edge and face orientations. While both reinforcements in the face orientation improve the fatigue resistance of γ-TiAl, the cyclic toughening increment is clearly greater for the Nb phase than for TiNb. The fatigue threshold for the Nb/TiAl composite, $\Delta K_{TH} \sim 10\ MPa\sqrt{m}$, is about 75 and 40% larger than the pure γ-TiAl ($\sim 6\ MPa\sqrt{m}$) and the TiNb/TiAl composite ($\sim 8\ MPa\sqrt{m}$), respectively. This is in contrast to fracture toughness behavior under monotonic loading, where the high-strength TiNb reinforcements are significantly more effective in impeding crack advance. When compared at a fixed ΔK of $10\ MPa\sqrt{m}$, growth rates are nearly five orders of magnitude

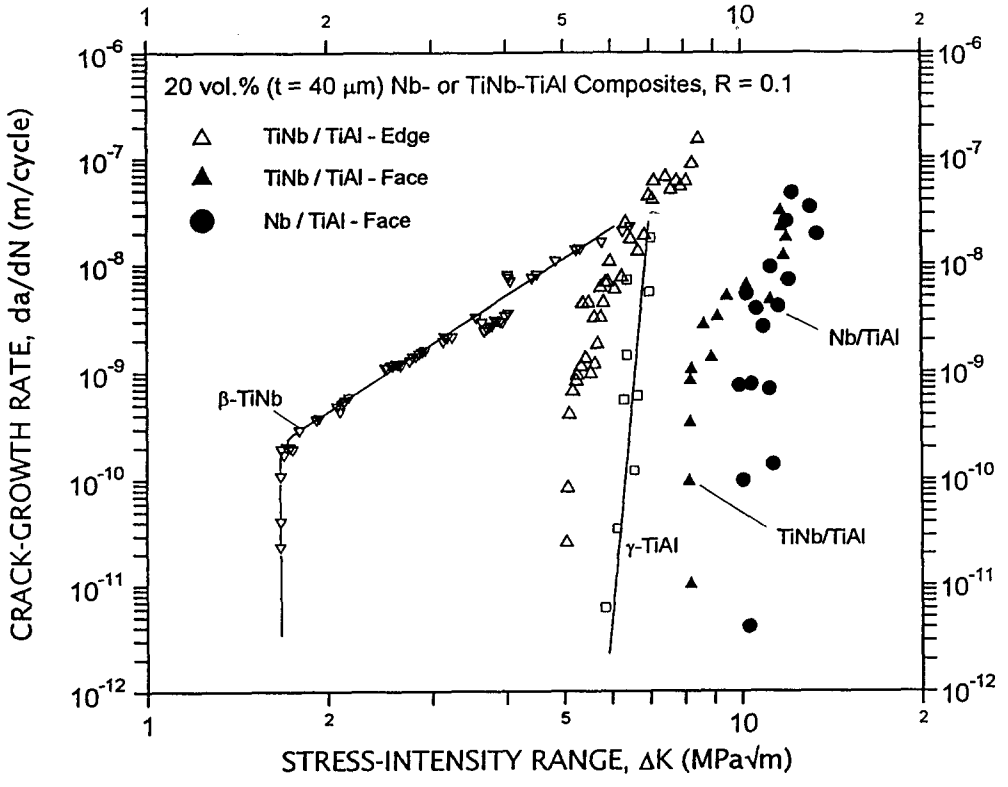

Fig. 17. Effect of Nb vs TiNb ductile reinforcements on the cyclic crack-growth resistance of γ-TiAl in the face (C–L) orientation ($R = 0.1$). Note the superiority of Nb/γ-TiAl composites due to their relatively weak interfacial bonding compared to TiNb/γ-TiAl.

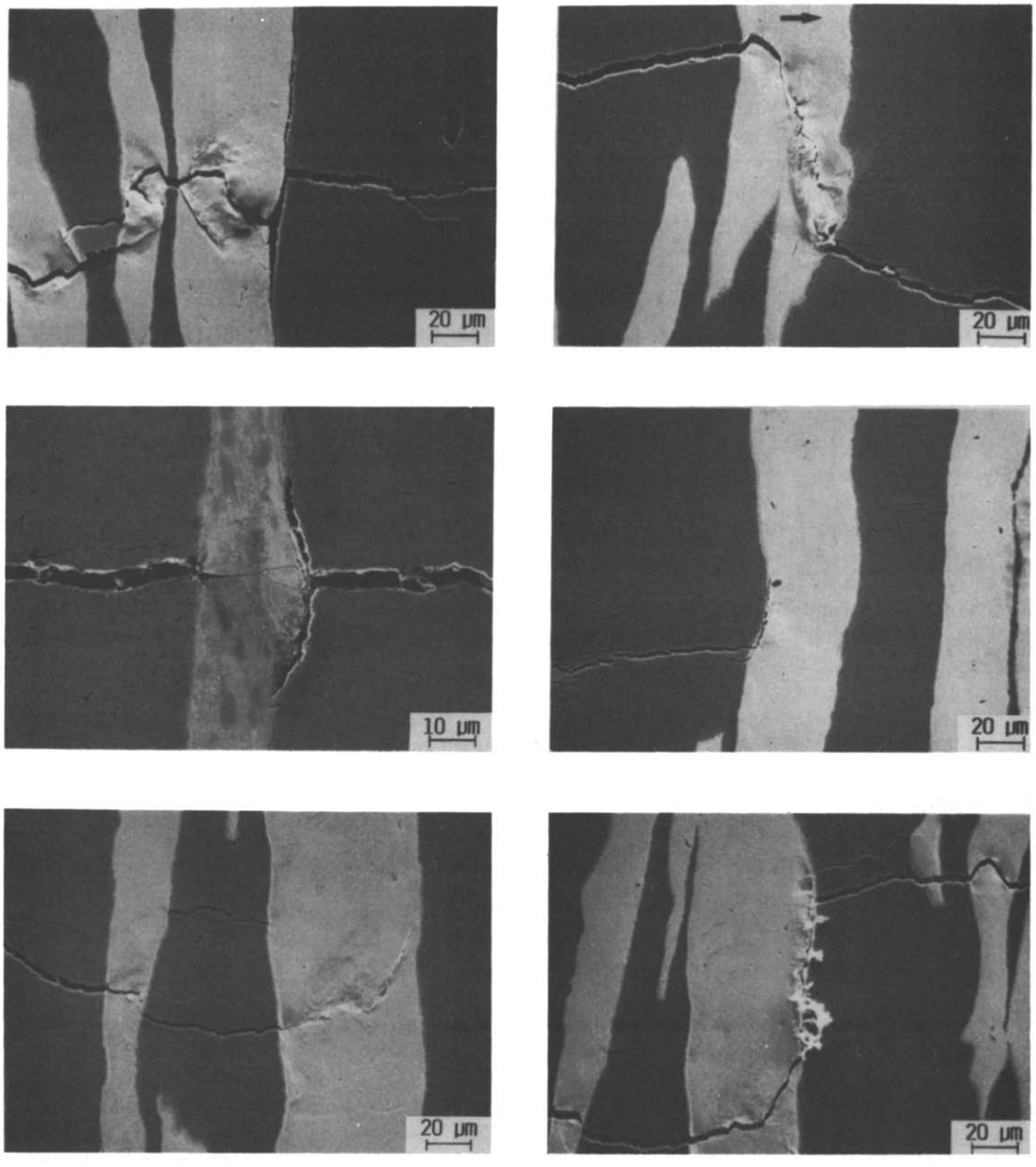

Fig. 18. Summary of cyclic crack-path morphologies (in the plane of loading) observed for the Nb/γ-TiAl composite in the face (C–L) orientation, showing significant interfacial debonding, cracking ahead of the Nb particles and evidence of crack bridging. Horizontal arrow represents the crack-growth direction.

slower in Nb/TiAl than in TiNb/TiAl. However, the enhancement in fatigue resistance of γ-TiAl from Nb additions is far less compared to that equivalent increase in fracture toughness [Fig. 9(c)].

Such improved fatigue-crack growth properties using Nb reinforcements can be traced to significant secondary-cracking effects locally near the Nb/TiAl interface. As illustrated in Fig. 18, these are characterized by (i) crack arrest at the interface, (ii) decohesion along the interface and (iii) crack renucleation in the brittle matrix ahead of the particle, prior to particle failure. Analogous to behavior under monotonic loads, the brittle σ-layer interface surrounding Nb particles is expected to be less fatigue resistant and susceptible to debonding compared to the ductile α_2 layer around TiNb particles. Nevertheless, such debonding at the Nb/TiAl interface relaxes constraint, diffuses plastic strains, and prevents continuous crack penetration into the ductile Nb phase; these mechanisms, in addition to crack renucleation which preserves *local* crack-tip bridging, extend the fatigue life of the Nb reinforcements. However, the extent of debonding during fatigue is less than that seen under monotonic loading (Fig. 10) and is much more evident in Nb/TiAl. Conversely, debonding is not evident for TiNb/TiAl composites under fatigue, as under monotonic loading, and consequently the cracks advanced continuously through the α_2 layer

into the TiNb particle without significant interfacial interactions, thereby leading to rapid failure of the TiNb phase. Moreover, the TiNb phase is inherently more susceptible to fatigue failure in fewer cycles (due to localized planar-slip deformation) than the strain-hardening Nb phase, consistent with previous results. (Note that fatigue-crack growth rates in Nb are also strongly dependent on interstitial H_2, C, N_2, O_2, and Si impurity contents [26].)

Finally, it is useful to estimate the magnitude of toughening associated with various mechanisms under cyclic loading to provide some insight into their relative contributions. The effects of local crack bridging in fatigue (Fig. 18), specifically in the face orientation, on the reduction in near-tip stress intensity, ΔK_b, may be assessed using the Dugdale approximation [27]

$$\Delta K_b = \frac{2}{\sqrt{\pi}} f\sigma_e \sqrt{2L_b} \tag{8}$$

where, L_b is the bridging-zone length and σ_e the effective value for uniform bridging tractions in that zone. Taking $L_b \sim 40\,\mu$m (bridging zone $\sim$ reinforcement thickness) and the average bridging tractions under cyclic loading to be roughly one half the flow stress ($\sigma_e \sim 0.5[\sigma_0 + \sigma_u]/2$, or $\sim$215 and $\sim$100 MPa for TiNb and Nb, respectively), the in-plane bridging contributions, ΔK_b, for a composite reinforced with 20 vol.% ductile particles are a mere $\sim$0.4 and $\sim$0.2 MPa$\sqrt{\text{m}}$ for TiNb and Nb phases, respectively. Measured shifts in the da/dN–ΔK curves (Fig. 17) are, respectively, $\sim$2 and $\sim$4 MPa$\sqrt{\text{m}}$ for the TiNb/TiAl and Nb/TiAl composites, implying that other mechanisms are relevant. Crack trapping and renucleation of the fatigue crack in the ductile phase associated with blunting (via interfacial decohesion for Nb), and coplanar bridging from multiple and discontinuous crack fronts (for TiNb and Nb) are expected to provide the additional contributions to the fatigue-crack growth resistance.

4. CONCLUDING REMARKS

The present results extend previous studies [15, 16] in illustrating the contrasting role of ductile reinforcements on monotonic (fracture toughness) and cyclic (fatigue) crack-growth resistance of intermetallic-matrix composites. With respect to R-curve toughness, the principal factors are effective reinforcement strength and ductility as mediated by constraint imposed by debonding characteristics of the interface and resultant constrained deformation properties of the reinforcement; local crack/particle interactions contribute to intrinsic crack-initiation toughness. Reinforcement thickness (initiation toughness) and orientation (edge vs face) effects on toughness, previously seen in coarse laminated composites, appear to be modest for the pancake-shaped ductile-phase toughened composites, suggesting competing effects of various local crack/particle interactions on monotonic crack-growth resistance.

Very different mechanisms and microstructural factors are associated with fatigue-crack propagation resistance. This is perhaps best illustrated by the degradation in fatigue thresholds compared to γ-TiAl and accelerated crack-growth rates relative to either monolithic constituent in the edge-oriented TiNb/TiAl composites, particularly at low volume fractions. The premature cracking or low-cycle fatigue failure of ductile particles at small crack-opening displacements under cyclic loading result in very limited bridging zones and therefore minimal toughening. Improved fatigue resistance is seen only in the face-oriented composites, the increase being attributed to local crack-particle interaction mechanisms that are similar to those under monotonic loading, yet are far less potent under cyclic loading. The fatigue resistance of the composites is further enhanced by weak (debonding) particle–matrix interfaces and ductile particles with optimal fatigue properties, e.g. strain-hardening phases with high modulus and strength. Debonding can be induced at inherently strong reaction-layer interfaces by applying thin oxide coatings between constituents, although this can reduce the toughness. These observations suggest that ductile phases are associated with multiple and competing mechanisms, with the net effect under fatigue loading being sensitive to reinforcement architecture, volume fraction and particle thickness.

Such differing, and in some cases contradictory, requirements for superior toughness and fatigue resistance suggest that optimized composite microstructures may require a variety of reinforcements and architectures based on alternative shielding mechanisms. For example, a semi-continuous network of the ductile phase offering a preferred crack path may provide improved fatigue resistance by promoting crack meandering. This in turn promotes crack-tip shielding from roughness-induced crack closure by wedging of enlarged fracture-surface asperities, and has proved to be very effective in improving the fatigue-crack growth resistance of duplex ferritic/martensitic steels and α/β titanium alloys [28, 29]. Such an approach should also provide adequate toughness under monotonic loads due to the formation of extensive bridging zones.

5. CONCLUSIONS

Based on an experimental study of the monotonic and cyclic crack-growth properties of ductile-phase toughened γ-TiAl intermetallic composites, reinforced with either β-TiNb or Nb, the following conclusions can be made:

1. Brittle γ-TiAl intermetallic alloys can be significantly toughened under monotonic loading by dispersing ductile Nb or TiNb reinforcements; compared to a fracture toughness of 8 MPa$\sqrt{\text{m}}$ for pure γ-TiAl, both type of composites show increased

crack-initiation toughness (K_i) and marked resistance-curve behavior with $K_r(\Delta a)$ values in excess of $\sim 40\ \mathrm{MPa}\sqrt{\mathrm{m}}$. Under monotonic loading, the stronger β-TiNb particles impart greater toughening than Nb reinforcements.

2. Improvement in crack-growth toughness (as reflected by the resistance-curve slope, dK_r/da) under monotonic loading is primarily attributed to shielding effects, associated with extensive bridging by intact TiNb or Nb ligaments, over dimensions of several millimeters, in the crack wake. A number of local crack-particle interactions enhance the crack-initiation toughness, and provide secondary contributions to crack-growth toughness. Depending on the measure, toughness increases with thickness (K_i) and volume fraction (K_i, dK_r/da) of the ductile-phase particles; however, reinforcement orientation appears to have a relatively minor effect.

3. Ductile TiNb and Nb reinforcements also lead to enhanced cyclic fatigue-crack growth resistance of γ-TiAl, although the effect is specific *only* to the face (C–L) orientation and is seen as a modest increase in the fatigue threshold, ΔK_{TH}. The increase appears to be associated with local crack–particle interaction mechanisms, including crack renucleation (in the matrix and/or particle), crack branching, limited interface debonding and discontinuous (out-of-plane) crack bridging.

4. Conversely in the edge (C–R) orientation, TiNb particles actually *degrade* the ΔK_{TH} relative to γ-TiAl, and at low volume fractions accelerate the intermediate crack-growth rates relative to *either* monolithic constituents. Behavior is primarily due to the premature fatigue fracture of ductile phases under cyclic loads, which severely limits bridging in the crack wake, and the absence of any other microstructural interactions.

5. In direct contrast to their effect on toughness under monotonic loading, in the face (C–L) orientation, Nb particles yield better fatigue-crack growth resistance compared to TiNb particles. This results from extensive debonding of Nb particles from the γ-TiAl matrix, due to the weak Nb/TiAl interface, and their inherently better fatigue properties compared to TiNb reinforcements.

Acknowledgements—This work was supported by the U.S. Air Force Office of Scientific Research under Grant No. AFOSR-90-0167 (KTVR and ROR), and by the Defense Advanced Research Projects Agency under Contract No. URI-N00014-86-K-0753 (GRO). Thanks are due to Dr Alan H. Rosenstein for his continued support, Pratt and Whitney for provision of materials, Professor G. E. Lucas, Dr R. H. Dauskardt for helpful discussions, and J. W. Sheckherd, C. Liu, C. Muhlstein and D. Nath for experimental assistance.

REFERENCES

1. C. T. Liu, J. O. Stiegler and F. H. Froes, *Metals Handbook* **2,** 913 (1991).
2. R. L. Fleischer, D. M. Dimiduk and H. A. Lipsitt, *Ann. Rev. Mater. Sci.* **19,** 231 (1989).
3. Y. W. Kim, *Acta metall. mater.* **40,** 1121 (1992).
4. Y. W. Kim and D. M. Dimiduk, *J. Metals* **43(8),** 40 (1991).
5. K. S. Chan and Y. W. Kim, *Metall. Trans. A* **23A,** 1663 (1992).
6. K. S. Chan, *J. Metals* **44(5),** 30 (1992).
7. H. E. Dève, A. G. Evans and D. S. Shih, *Acta metall. mater.* **40,** 1259 (1992).
8. C. K. Elliott, G. R. Odette, G. E. Lucas and J. W. Sheckherd, in *High-Temperature/High-Performance Composites* (edited by F. D. Lemkey, A. G. Evans, S. G. Fishman and J. R. Strife), MRS Symp. Proc., Vol. 120, p. 95. MRS, Pittsburgh, Pa (1988).
9. H. E. Dève, A. G. Evans, G. R. Odette, R. Mehrabian, M. L. Emiliani and R. J. Hecht, *Acta metall. mater.* **38,** 1491 (1990).
10. G. R. Odette, H. E. Dève, C. K. Elliott, A. Hasegowa and G. E. Lucas, in *Interfaces in Ceramic Metal Interfaces* (edited by R. Y. Lin, R. J. Arsenault, G. P. Martins and S. G. Fishman), p. 443. TMS-AIME, Warrendale, Pa (1990).
11. G. R. Odette, B. L. Chao, J. W. Sheckherd and G. E. Lucas, *Acta metall. mater.* **40,** 2381 (1992).
12. V. D. Krstic, P. S. Nicholson and R. G. Hoagland, *J. Am. Ceram. Soc.* **64,** 499 (1981).
13. M. F. Ashby, F. J. Blunt and M. Bannister, *Acta metall.* **37,** 1847 (1989).
14. B. D. Flinn, M. Rühle and A. G. Evans, *Acta metall.* **37,** 3001 (1989).
15. K. T. Venkateswara Rao, G. R. Odette and R. O. Ritchie, *Acta metall. mater.* **40,** 353 (1992).
16. K. T. Venkateswara Rao and R. O. Ritchie, in *Intermetallic Matrix Composites II* (edited by D. Miracle, J. Graves and D. Anton), MRS Symp. Proc., Vol. 273, p. 127. MRS, Pittsburgh, Pa (1992).
17. A. Hasegowa, G. E. Lucas and G. R. Odette, unpublished results, Univ. of California, Santa Barbara (1992).
18. American Society for Testing and Materials Standard E399-90, 3.01, 506 (1992).
19. R. O. Ritchie and R. H. Dauskardt, *J. Ceram. Soc. Japan* **99,** 1047 (1991).
20. R. H. Dauskardt and R. O. Ritchie, *Closed Loop* **27,** 7 (1989).
21. American Society for Testing and Materials Standard E647-91, 3.01, 674 (1992).
22. R. O.Ritchie, W. Yu and R. J. Bucci, *Engng Fract. Mech.* **32,** 361 (1989).
23. M. Y. He, F. E. Heredia, D. J. Wissuchek, M. C. Shaw and A. G. Evans, *Acta metall. mater.* **41,** 1223 (1993).
24. R. O. Ritchie, *Int. Metall. Rev.* **20,** 205 (1979).
25. K. T. Venkateswara Rao and R. O. Ritchie, *Int. Mater. Rev.* **37,** 153 (1992).
26. S. Fariabi, A. L. W. Collins and K. Salama, *Metall. Trans. A* **14A,** 701 (1983).
27. H. Tada, P. C. Paris and G. R. Irwin, *The Stress Analysis of Cracks Handbook*, Paris Prod. Inc./Del Corp., St Louis, Mo. (1985).
28. J.-K. Shang, J. L. Tzou and R. O. Ritchie, *Metall. Trans. A* **18A,** 1613 (1987).
29. J. M. Larsen, T. Nicholas, A. W. Thompson and J. C. Williams, in *Small Fatigue Cracks* (edited by R. O. Ritchie and J. Lankford), pp. 499–512, T.M.S.-A.I.M.E., Warrendale, Pa (1986).